catalysts

MDPI

Article

Mechanistic Studies into the Selective Production of 2,5-furandicarboxylic Acid from 2,5-bis(hydroxymethyl)furan Using Au-Pd Bimetallic Catalyst Supported on Nitrated Carbon Material

Yiran Liu [1], Yao Chen [2], Wen Guan [1], Yu Cao [1], Fang Wang [1] and Yunlei Zhang [1,*]

[1] Institute of Green Chemistry and Chemical Technology, School of Chemistry and Chemical Engineering, Jiangsu University, Xuefu Road 301, Zhenjiang 212013, China
[2] School of the Environment and Safety, Jiangsu University, Xuefu Road 301, Zhenjiang 212013, China
* Correspondence: jsdxzyl@ujs.edu.cn

Abstract: Aerobic oxidation of bio-sourced 2,5-bis(hydroxymethyl)furan (BHMF) to 2, 5-furandicarboxylic acid (FDCA), a renewable and green alternative to petroleum-derived terephthalic acid (TPA), is of great significance in green chemicals production. Herein, hierarchical porous bowl-like nitrogen-rich (nitrated) carbon-supported bimetallic Au-Pd nanocatalysts (Au_mPd_n/ N-BN_xC) with different nitrogen content and bimetal nanoparticle sizes were developed and employed for the highly efficient aerobic oxidation of BHMF to FDCA in sodium carbonate aqueous solution. The reaction pathway for catalytic oxidation of BHMF went through the steps of BHMF→HMF→HMFCA→FFCA→FDCA. Kinetics studies showed that the activation energies of BHMF, HMF, HMFCA, and FFCA were 58.1 kJ·moL^{-1}, 39.1 kJ·moL^{-1}, 129.2 kJ·moL^{-1}, and 56.3 kJ·moL^{-1}, respectively, indicating that the oxidation of intermediate HMFCA to FFCA was the rate-determining step. ESR tests proved that the active species was a superoxide radical. Owing to the synergy between the nitrogen-rich carbon support and bimetallic Au-Pd nanoparticles, the Au_1Pd_1/N-BN_2C nanocatalysts exhibited BHMF conversion of 100% and FDCA yield of 95.8% under optimal reaction conditions. Furthermore, the nanocatalysts showed good stability and reusability. This work provides a versatile strategy for the design of heterogeneous catalysts for the highly efficient production of FDCA from BHMF.

Keywords: 2,5-bis(hydroxymethyl)furan; 2,5-furandicarboxylic acid; aerobic oxidation; nitrogen-doped carbon; bimetallic Au-Pd nanoparticles

Citation: Liu, Y.; Chen, Y.; Guan, W.; Cao, Y.; Wang, F.; Zhang, Y. Mechanistic Studies into the Selective Production of 2,5-furandicarboxylic Acid from 2,5-bis(hydroxymethyl)furan Using Au-Pd Bimetallic Catalyst Supported on Nitrated Carbon Material. *Catalysts* **2023**, *13*, 435. https://doi.org/10.3390/catal13020435

Academic Editors: Indra Neel Pulidindi, Aharon Gedanken and Pankaj Sharma

Received: 27 December 2022
Revised: 14 February 2023
Accepted: 15 February 2023
Published: 17 February 2023

1. Introduction

Dwindling fossil stocks and increased environmental awareness have triggered a rush to find renewable resources [1]. Biomass, derived from plant photosynthesis, is a new source of cheap, available, and renewable energy and has been widely used to produce high value-added fuels and chemicals [2–4]. Biomass has been identified as an ideal candidate for the development of sustainable energy and value-added materials that can partially replace current petrochemicals [5]. Therefore, research and development of renewable biomass are of great significance and urgent need. 5-hydroxymethylfurfural (HMF) is a biomass-based platform compound containing active aldehyde, hydroxyl, and furan ring structures. Through further reaction, many downstream products can be derived from HMF, which is a crucial intermediate connecting biomass chemistry and petrochemistry. Among them, 2,5-furandicarboxylic acid (FDCA) was the sole aromatic molecule among the "twelve platform bio-based compounds" that the U.S. Department of Energy presented back in 2004 and was subsequently significantly used in the synthesis of polyester, polyamide, epoxy resin, and other polymers [6–8]. FDCA is considered as an ideal substitute for the petroleum derivative terephthalic acid (TPA) due to its similar physical and chemical

properties. In addition, compared to TPA-derived polyethylene terephthalate (PET), the bio-based polyester 2,5-furandicarboxylate (PEF) produced by FDCA has better gas insulation, thermal stability, and mechanical properties, and FDCA has broad application prospects and high market potential [9–12].

Due to the great potential of FDCA, a variety of catalysts for FDCA production from HMF have been developed in recent years [13–15]. In previous studies, homogeneous and heterogeneous catalysts were used for the catalytic production of FDCA. It is difficult to separate the homogeneous catalysts from the reaction medium, and their stability and recyclability are poor. The study of heterogeneous catalysts has greater commercial potential and practical application as well [16]. At present, most research on catalytic oxidation for FDCA preparation is focused on supporting precious metals (Pt [17], Au [18,19], Pd [20,21], and Ru [16,22]) on multiphase catalysts. Davis et al. found that Au-based catalysts have strong aldehyde oxidation activity in alkaline circumstances [23]. Lei et al. found that palladium is more favorable for the oxidation of alcohols [24]. Combining the advantages of Au and Pd, the preparation of a bimetallic catalyst for FDCA with high activity, high selectivity, and high stability through catalytic oxidation of HMF is of great significance [25,26]. Although significant progress has been made in this regard [27–30], HMF is thermally and chemically unstable, often leading to severe degradation that hinders its storage and industrialization. To solve this problem, an alternative pathway is used, in which the 2,5-bis(hydroxymethyl)furan (BHMF) is first converted to HMF and then oxidized to produce FDCA. Because of the better storage stability of BHMF, the BHMF-mediated pathway has a brighter future for FDCA mass production [1,17,29].

The carrier in the supported metal catalyst not only disperses and stabilizes the metal nanoparticles, but the synergistic interaction between the carrier and the metal particles also leads to interfacial charge transfer, metal structure change, molecular adsorption modulation, and other phenomena, thus affecting the activity, selectivity, and stability of the catalyst. Carbon materials are promising supports for metal nanoparticles, especially fuel cell catalysts and catalysts for reactions in aqueous medium, due to their high stability over a wide pH range and the ease of surface functionalization through the incorporation of other elements, such as oxygen and nitrogen [31–33]. In general, for faster reaction rates and better product solubility, selective BHMF oxidation must be carried out in more alkaline conditions. However, use of strong alkalis will make it hard to separate the finished product, which will cause the active phase to leak out of the reactor and will result in corrosion [34]. In our previous study, nitration improved the adsorption capacity of the substrate, allowing the reaction substrate to more easily come into contact with the active site on the catalyst surface and improving the desorption ability of the product (FDCA) [35]. Nitrogen-doped carbon materials show excellent performance in the field of catalysis, which is expected to become a forward-looking field of catalyst development and promote the progress of related industrial technology [7]. In this study, nitrogen-doped carbon material after nitrification, which can provide basic sites, was used as support to synthesize a highly efficient catalyst. Due to the introduction of nitrogen, nitrogen-doped carbon materials have a special structure and have more advantages than traditional catalysts [36]. The nitrogen doping process can introduce defect sites and nitrogen species, improve the physical and chemical properties of catalysts, and interact with active species to improve catalytic performance. The interaction between nitrogen species and active components, such as metal components or metal oxides, can effectively improve the dispersion and stability of active species and adjust their redox properties, thus realizing improvements in catalytic performance [37].

In this work, hierarchical porous bowl-like nitrogen-rich carbon-supported bimetallic Au-Pd nanocatalysts (Au_mPd_n/N-BN_xC) were synthesized by precipitation polymerization employing uniform silica nanospheres as a template, which was followed by carbonization, removal of SiO_2 spheres, and loading of Au-Pd bimetallic procedures. Au_mPd_n/N-BN_xC catalysts were obtained by adjusting the polymerization ratio and Au-Pd ratio. The catalysts were characterized by TEM, XRD, TGA, SEM, Raman spectroscopy, FT-IR spectroscopy, N_2

adsorption/desorption isotherms, and XPS, and catalytic reactive species were determined by ESR spectroscopy. Through aerobic oxidation of BHMF to FDCA experiments, the influences of nitrogen content and metal ratio on the catalytic performance of catalysts were explored, and the influences of reaction factors such as time, temperature, and pressure were considered. The catalytic performance of the catalyst was elucidated. The possible reaction pathway and catalytic mechanism were proposed. Finally, the stability and reusability of the catalyst were evaluated through cyclic experiments. An alternative pathway was used to solve the problem regarding hydroxymethylfurfural being unstable in heat and chemistry, which often resulted in serious degradation. This is of great significance to the industrial production of FDCA.

2. Results and Discussion

2.1. Preparation and Characterization of the Au_mPd_n/N-BN_xC Nanocatalysts

As shown in Scheme 1, employing SiO_2 nanospheres as a template, Au_mPd_n/N-BN_xC nanocatalysts were prepared via precipitation polymerization, carbonization, SiO_2 sphere removal, nitrification, and the loading of Au-Pd bimetal nanoparticles. According to the SEM image of Figure 1a and Figure S1, compared to the smooth surface before polymerization, an uneven flower-like polymerization layer appeared on the surface after polymerization, showing that the precipitation polymerization effectively covered SiO_2 spheres. By altering the proportion of AM and MBA monomers (1:1, 2:1, 3:1), polymers with different nitrogen content were obtained. As shown in Figure 2(a1–a3), it was observed that the thickness of the polymerization layer changed obviously with the adjustment of the proportion of polymerization monomer. The polymer layer was then carbonized via calcination at 800 °C under the protection of nitrogen, and the SiO_2 nanospheres (SiO_2@N_xC) were wrapped by a thin and uniform nitrogen-doped carbon shell.

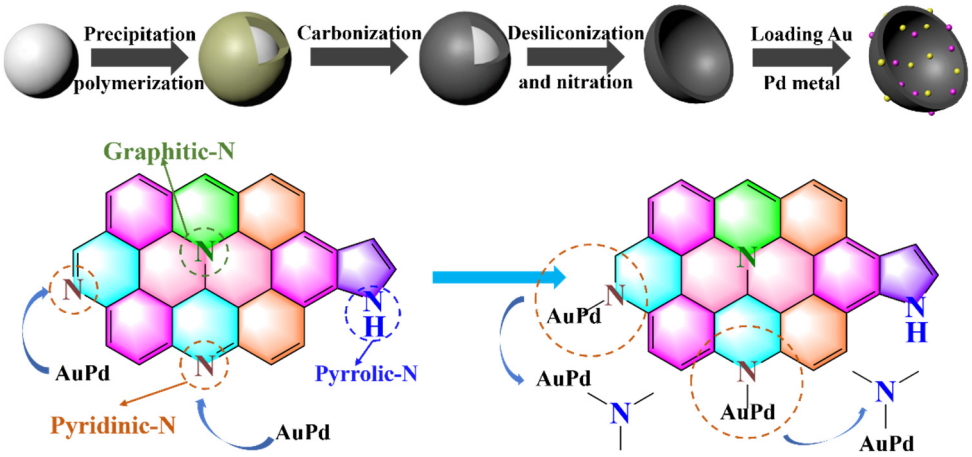

Scheme 1. Schematic illustration for preparing Au_mPd_n/N-BN_xC nanocatalysts.

To obtain the porous structure, the SiO_2 template was removed with hydrofluoric acid. The porous structure can be clearly seen in the SEM (Figure 1b) and TEM (Figure 2(b1–b3)) images. The porous bowl structure had a very large contact area with the substrate, named BN_xC, which effectively improved the adsorption of the substrate. However, the contact angle test found that the carrier had superhydrophobicity at this time (Figure S2). On this basis, the carrier was treated with nitric acid to weaken its hydrophobicity, and N-BN_xC was obtained (Figures 1c and 2(c1–c3)). Finally, the bimetal was loaded onto the carrier using the injection reduction method, and the final samples were named Au_mPd_n/N-BN_xC. TEM images showed that the metal particles had been successfully loaded [7]. The metal nanoparticles were well dispersed across the surface of the carrier, as shown in Figure 2(d1–d3), and the particle sizes of the metal particles with different polymerization thicknesses were also different. The average metal particle size of Au_1Pd_1/N-BN_1C, Au_1Pd_1/N-BN_2C, and Au_1Pd_1/N-BN_3C was 11.26, 10.65, and 11.88 nm, respectively.

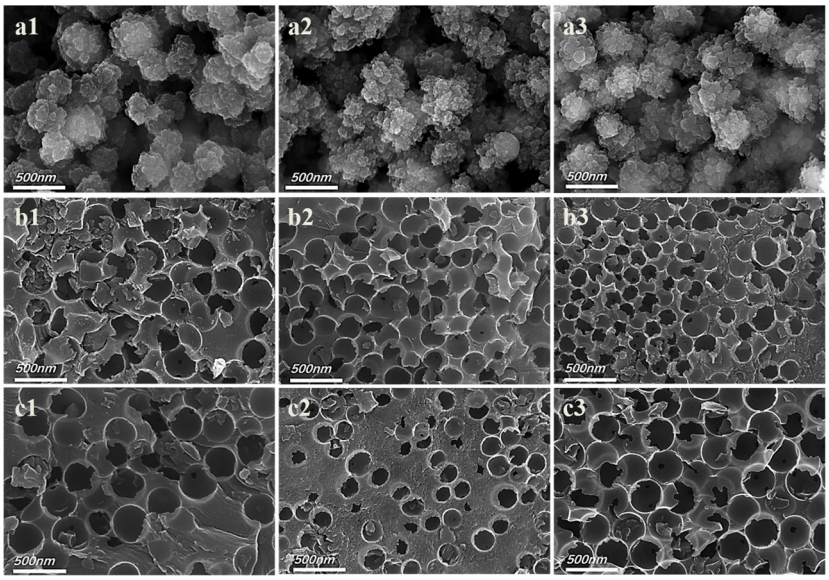

Figure 1. SEM images of SiO_2@N_xP (**a1–a3**), BN_xC (**b1–b3**), and N-BN_xC (**c1–c3**) (x = 1, 2, 3, corresponding to MBA:AM = 1:1, 1:2, 1:3, respectively).

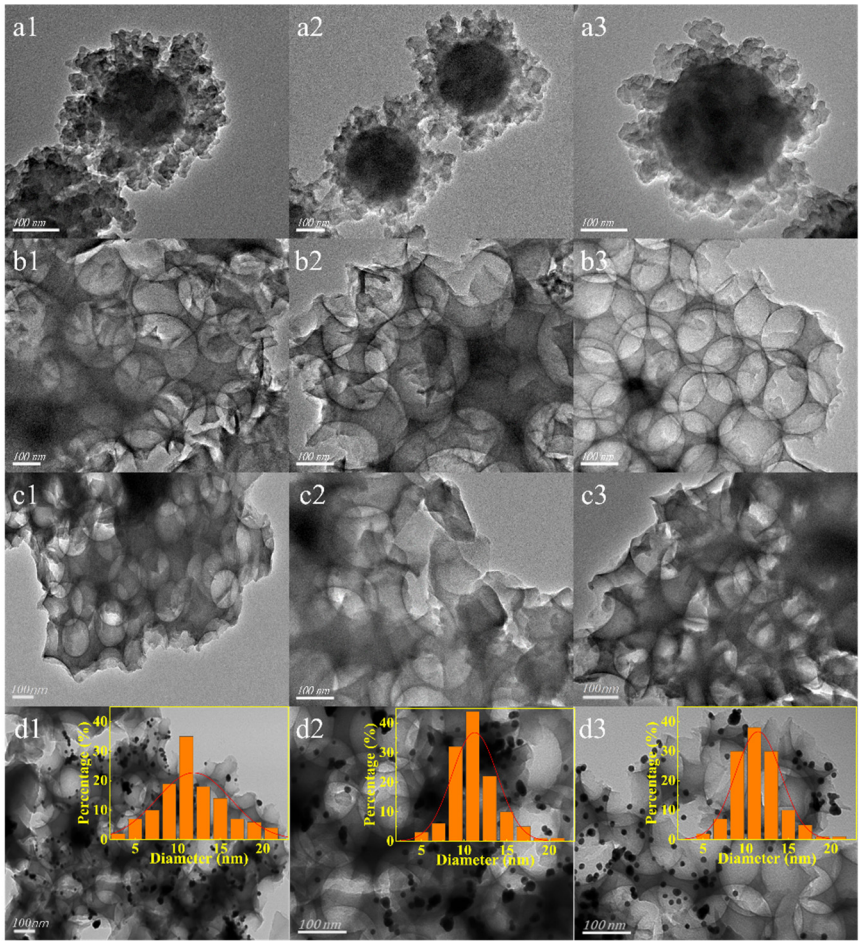

Figure 2. TEM images of SiO_2@$Poly_x$ (**a1–a3**), BN_xC (**b1–b3**), N-BN_xC (**c1–c3**), and Au_1Pd_1/N-BN_xC (**d1–d3**) nanocatalysts (x = 1, 2, 3, corresponding to MBA:AM = 1:1, 1:2, 1:3, respectively).

Furthermore, the components of the representative Au_1Pd_1/N-BN_2C nanocatalyst were characterized by HR-TEM, SAED, and EDS. HR-TEM images (Figure 3a,b) of Au_1Pd_1/N-BN_2C showed the crystal planes of Pd (111), Pd (200), and Au (311), which were 0.2219 nm,

0.2034 nm, and 0.1153 nm, respectively. In addition, selective electron diffraction (SAED) of the Au_1Pd_1/N-BN_2C catalyst (Figure 3c) also showed the (111), (200), and (311) crystal faces of Au and Pd, respectively. The representative Au_1Pd_1/N-BN_2C nanocatalyst was composed of C, N, O, Au, and Pd elements (Figure 3d). Moreover, the bimetallic nanoparticles were uniformly loaded on the support surface (Figure 3e–i).

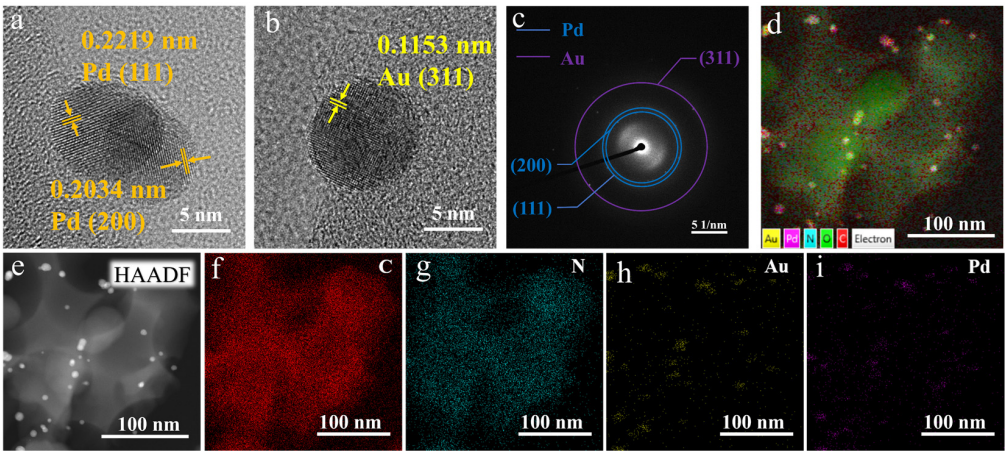

Figure 3. HR-TEM (**a**,**b**), SAED (**c**), EDS (**d**), HAADF (**e**) and element mapping images(**f**–**i**) of the representative Au_1Pd_1/N-BN_2C nanocatalysts.

A nitrogen adsorption–desorption experiment was used to investigate the pore size distribution and BET specific surface area of materials. As shown in Figure 4, the H4 hysteresis loop could also be seen in the adsorption and desorption isotherms [38], indicating the existence of a cavity in BN_xC and N-BN_xC carriers. Correspondingly, it could be clearly seen in the transmission diagram of Figure 2 that there were indeed many holes. According to the adsorption data, the pore size of the N-BN_xC sample was similar, while the pore size of the BN_3C sample was slightly different from that of BN_1C and BN_2C. Table 1 shows the pore structure data of different catalysts. By comparing the data of different carriers, the specific surface area decreased from 53.9, 35.1, and 119 to 9.4, 13.2, and 11.4 m^2g^{-1} after nitric acid treatment. We speculate that nitrification alters the pore structure of carbon materials, resulting in a reduction in specific surface area and a change in pore size, but that the fundamental morphology of carbon materials remains largely unchanged. The porous structure improves the penetrability of the catalyst and the speed at which carriers transfer mass. According to the results of TEM, BET, and elemental analysis, it could be determined that porous nitrogen-doped carbon carriers were successfully prepared.

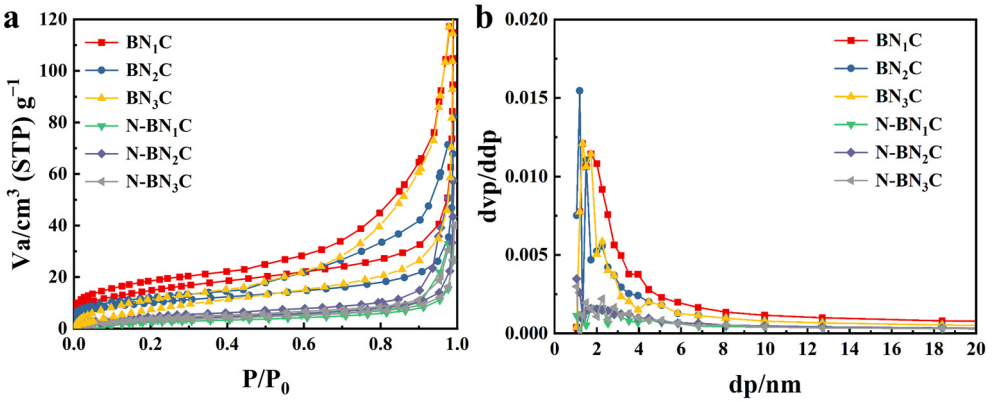

Figure 4. N_2 adsorption–desorption isotherms (**a**) and pore diameter distribution (**b**) of BN_xC and N-BN_xC (x = 1, 2, 3, corresponding to MBA:AM = 1:1, 1:2, 1:3, respectively).

Table 1. Pore structure and nitrogen content of BN_xC and N-BN_xC.

Samples	Surface Area [a] (m^2g^{-1})	Average Pore [a] (nm)	Pore Volume [a] (cm^3g^{-1})	Nitrogen Content [b] (%)
BN_1C	53.9	14.5	0.20	4.0
BN_2C	35.1	13.6	0.12	7.2
BN_3C	119	5.3	0.16	9.0
N-BN_1C	9.4	24	0.06	9.7
N-BN_2C	13.2	24.3	0.08	10.1
N-BN_3C	11.4	16.6	0.05	11.6

[a] Brunauer–Emmett–Teller (BET) surface area is determined by nitrogen adsorption and desorption isotherms. [b] Nitrogen content is calculated by elemental analysis.

To better understand the influence of the temperature of calcination on carbon morphology and whether nitrification also has an impact, Raman tests were conducted, as shown in Figure 5a. There were obvious peaks at 1350 m^{-1} and 1590 m^{-1}, which were the D and G bands of carbon [34]. The defect stretching vibration of the sp^3 carbon in support was visible in the D band, while the stretching vibration of the sp^2 carbon was visible in the G band [39]. The high I_D/I_G value indicated that the carbon frame structure had defects, which may be because of the structure breaking down due to the bowl structure formed by the removal of silica during the processing process. In addition, the defect concentration of the catalyst increased after nitrification, and the defect concentration of N-BN_2C was 1.1.

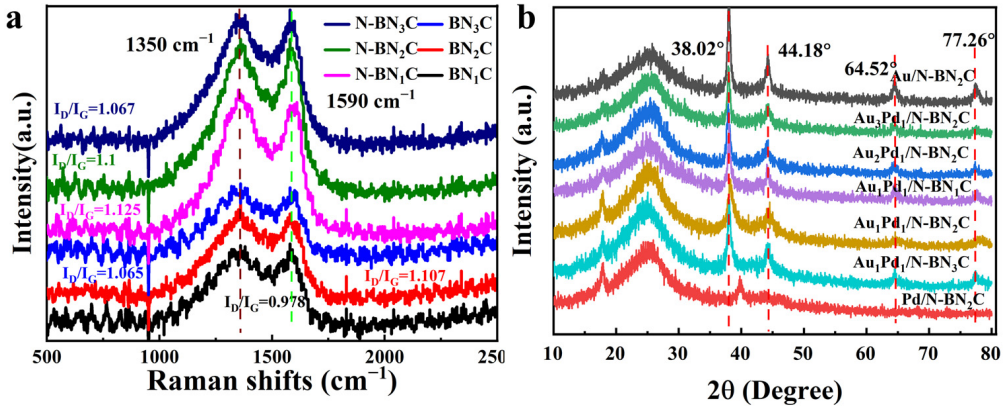

Figure 5. Raman spectra of BN_xC and N-BN_xC (**a**) and XRD spectra of Au_mPd_n/N-BN_xC (**b**) (x = 0, 1, 2, 3).

As shown in Figure 5b, XRD was used to characterize nitrifying samples under different AM:MBA and different Au:Pd ratios. Due to the high-temperature treatment of the sample, the polymer gel was graphitized during calcination; thus, diffraction peaks appeared at 17° and 25°, which were the (111) and (002) crystal planes of the graphite structure. XRD peaks appear at 38°, 44°, 64°, and 77° in the Au/N-BN_2C diagram, corresponding to the (111), (200), (220), and (311) crystal planes of Au. In the Pd/N-BN_2C diagram, XRD peaks appeared at 39° and 46°, corresponding to the (111) and (200) crystal planes of Pd [39,40]. It was found that the diffraction peaks of gold at 38° and 44° weakened, and the diffraction peaks at 64° and 77° almost disappeared when the two precious metals were grafted simultaneously. The diffraction peak of Pd overlapped with the diffraction peak of Au, indicating that the Au-Pd alloy had been successfully loaded. The successful synthesis of the Au-Pd alloy on support was confirmed by XRD.

In order to identify different types of nitrogen functional groups in catalysts, these materials were characterized by FT-IR analysis, as shown in Figure S3. To examine the chemical state and composition of the samples, XPS analysis was then performed. The XPS spectra of N 1s, C 1s, Pd 3d, and Au 4f orbits are shown in Figure 6. It can be seen that the binding energy peaks of the C–O bond and C–N bond of SiO_2@N_xP appeared at 288 eV and 285 eV, respectively. With carbonization, SiO_2 removal, and nitrification, their binding energies increased and their peak values decreased. For the C=C bond, the binding energy peak appeared at 284 eV, and there were no significant changes after subsequent treatment. However, the peak values of C–O and C–N bonds were increased when a single metal was loaded. In the N1s spectrum of SiO_2@N_xP, only the peak of quaternary-N (N-Q), with a binding energy of 400 eV, indicated that MBA and AM had been successfully introduced into the SiO_2 carrier. After calcination, SiO_2 removal, and nitrification, pyrrolic-N (N-5) and pyridinic-N (N-6) appeared, with binding energies of 404 eV and 398 eV, respectively [7]. The binding energies of quaternary-N were unchanged, and the peak value of pyridinic-N decreased slightly after nitrification. After loading the gold–palladium bimetal, the peak value of pyridinic-N decreased, but the peak value of quaternary-N and pyrrolic-N did not change obviously. The peak value of pyridine decreased while that of pyrrole-N increased with the loading of Au or Pd. The $4F_{5/2}$ and $4F_{7/2}$ binding energies of gold peaked at 87.85 eV and 84.15 eV, respectively. The binding energies for $3d_{5/2}$ and $3d_{3/2}$ in palladium peaked at 338 eV and 343 eV, respectively. The peaks of Au and Pd shifted to a higher energy level, and the N-5 and N-6 peaks changed to a lower level of energy. The results showed that there was an interaction between the metal and the support, which improved catalytic performance. The thermal stability of BN_xC and N-BN_xC was tested using the TG-DSC method. As shown in Figure S4, all the catalysts had relatively good thermal stability.

2.2. Catalytic Performance of Au_mPd_n/N-BN_xC Nanocatalysts

The transformation of BHMF with Au_1Pd_1/N-BN_2C was investigated regarding reaction time. As shown in Figure 7a, the yield of FDCA reached 95.8% after 24 h reaction. There were no significant changes in the FDCA yield when the reaction time was prolonged. Therefore, the reaction time was fixed at 24 h and other reaction conditions were discussed. Finally, it was discussed how the reaction pressure, temperature, and amount of catalyst affect the yield of FDCA (Figure S5). The catalytic activity of Au_1Pd_1/N-BN_2C was investigated in a variety of temperatures. When the reaction was carried out at 80 °C, the yield of FDCA was 30.2%. When the temperature was increased to 90 °C, the yield increased to 57.4%. The yield of FDCA approached 95.8% when the reaction temperature was gradually increased to 100 °C. Therefore, 100 °C was chosen as the reaction temperature. Additionally, the effect of oxygen pressure on the catalytic activity of the catalyst was also studied. With increasing oxygen pressure, FDCA yield increased from 40.8% (1.0 MPa) to 58.6% (1.5 MPa). The yield of FDCA increased to 95.8% when oxygen pressure was increased to 2.0 MPa. When pressure was further increased to 2.5 MPa, the production of FDCA did not change. In addition, the influence of the dosage of the catalyst on the catalytic activity of the catalyst was studied. The yield of FDCA increased from 43.8% (30 mg) to 70.6% (40 mg) with an increase in catalyst dose. The yield of FDCA improved to 95.8% when the catalyst dose was increased to 50 mg. The yield of FDCA dropped when the catalyst dose was increased to 60 mg. Therefore, the optimal conditions were 24 h treatment, 100 °C reaction temperature, 2.0 MPa oxygen pressure, and 50 mg of catalyst.

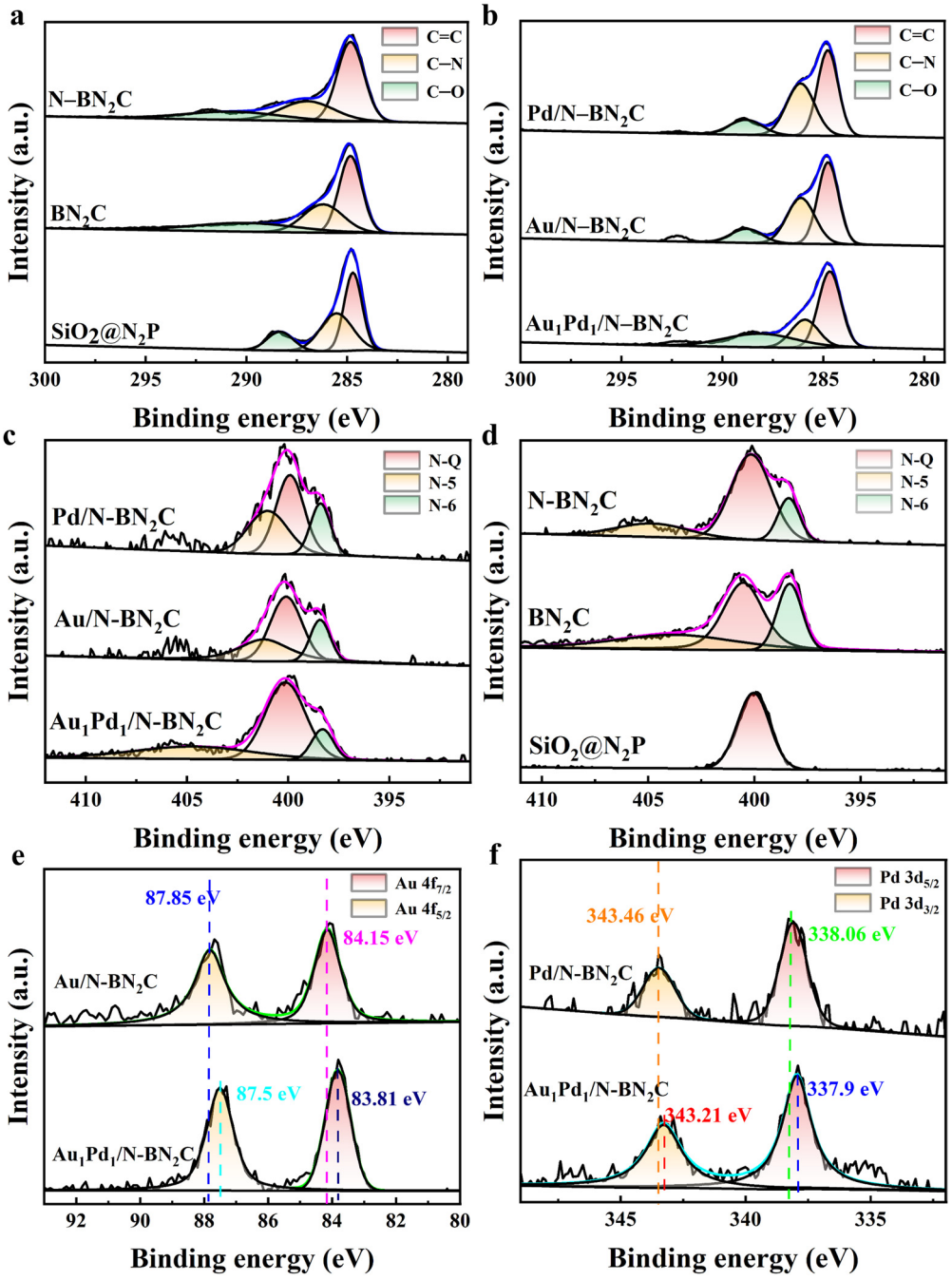

Figure 6. C 1s (**a**,**b**), and N 1s (**c**,**d**) XPS spectra of SiO_2@N_2P, BN_2C, N-BN_2C, Au/N-BN_2C, Pd/N-BN_2C, and Au_1Pd_1/N-BN_2C. Au 4f (**e**) and Pd 3d (**f**) XPS spectra of Au/N-BN_2C, Pd/N-BN_2C, and Au_1Pd_1/N-BN_2C.

The catalytic activity of Au_mPd_n/N-BN_xC nanocatalysts with different nitrogen content and gold–palladium ratios in the oxidation reaction from BHMF to FDCA was investigated, and Table 2 shows the results. The catalytic performance of the Au_1Pd_1/N-BN_2C nanocatalyst with moderate nitrogen content was the highest, and the Au_1Pd_1/N-BN_2C nanocatalyst could obtain the highest FDCA yield (95.8%). The thickness of the polymerization layer and the in situ doping of nitrogen could be adjusted using the polymerization method; thus, the thickness and nitrogen content of N-BN_xC could be adjusted. Nitrogen doping was able to interact with active species to enhance the adsorption of BHMF and improve catalytic performance. In our previous study, CO_2-TPD was used to detect basic sites on the surface of similar nanocatalysts, and the basic sites of materials increased with the increase in AM mole content [7]. Moreover, in the XPS analysis in Figure 6, the peak

of pyridine nitrogen can be observed. The catalyst had strong alkalinity due to its high pyridine nitrogen content. Thus, nitrogen doping also provided the bases that allowed the weak base to replace the strong base in the reaction. Nitrogen atoms also provide an anchor point for the metal particles, enhancing the interaction between the metal and the carrier. There was a significant interaction between Au and Pd in the bimetallic catalyst, which led to the achievement of 100% BHMF conversion and prominent FDCA yield under alkaline conditions. The recyclability of the catalyst was critical to this research and its performance was tested (Figure 7b). The catalytic performance of Au_1Pd_1/N-BN_2C decreased slightly, and both were able achieve to 100% BHMF conversion after five cycles, showing good stability. The recycled Au_1Pd_1/N-BN_2C was analyzed by TEM, XRD, Raman spectroscopy, and XPS, and the results are shown in Figures S6 and S7. It was also discovered that the support cracks and the metal particles decreased. We speculate that the loss of catalyst activity during the cycle may be due to metal shedding and support fragmentation.

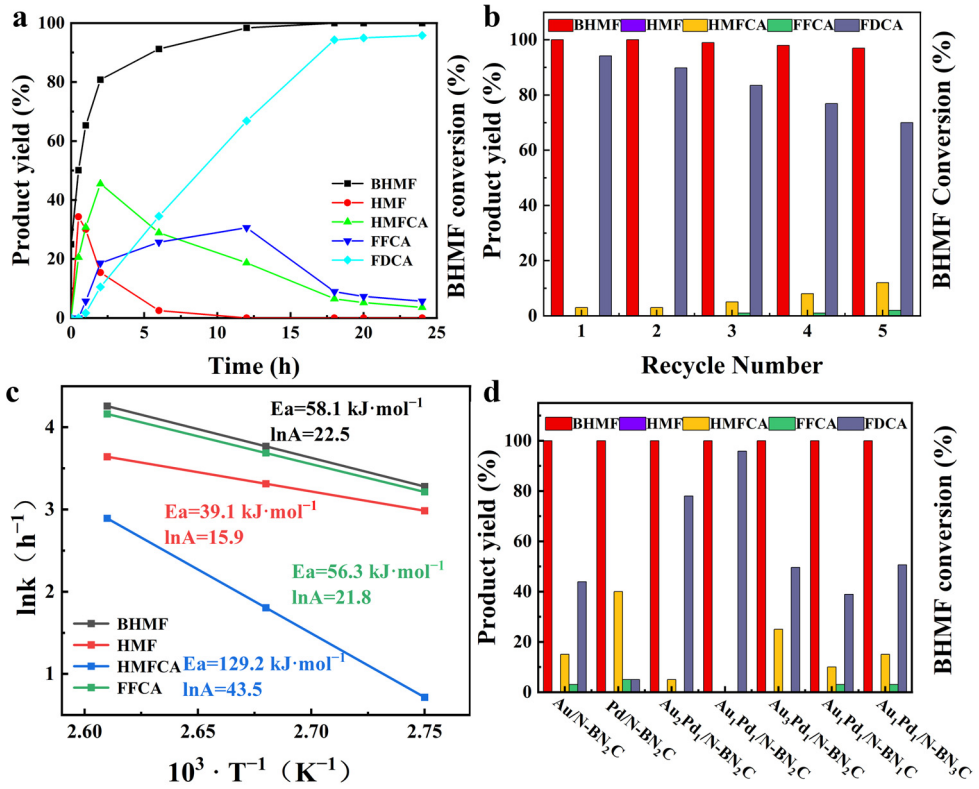

Figure 7. Effect of reaction time on the catalytic performance of the representative catalyst Au_1Pd_1/N-BN_2C-800 (**a**) and a study on the circulation of the optimal Au_1Pd_1/N-BN_2C nanocatalyst (**b**). Arrhenius plots of ln k based on different temperatures (**c**) and the catalytic oxidation performance of Au_mPd_n/N-BN_xC (**d**).

2.3. Kinetics and Catalytic Mechanism Studies

In the reaction process, we also detected that the intermediate substances were mainly HMF, 5-hydroxymethyl-2-furancarboxylic acid (HMFCA), and 5-formyl-2-furancarboxylic acid (FFCA), but we did not find any DFF. It could be speculated that the predicted reaction path is shown in Figure 8a. A kinetic model of BHMF transformation was proposed based on the summary of the previous experimental results, in which Ki represents different rate constants [7]. The influence of the concentration of BHMF and reaction temperature on the reaction rate was studied using the power function form of the kinetic reaction equation. The concentration of sodium carbonate was kept at 0.04 moL·L^{-1}; thus, the effect of sodium carbonate concentration on the reaction rate was ignored. Moreover, when the pressure of O_2 was higher than 3.0 MPa, the influence of O_2 pressure on the activity of the catalyst was almost zero; thus, its influence on the rate of reaction was ignored [7]. In the catalytic

reaction, a linear relationship between the BHMF conversion rate at 0.5 h and the amount of catalyst was discovered, and the kinetic reaction equation could be determined as:

$$r = \frac{dC_0}{dt} = kC_0^n \quad (1)$$

where k is the constant for the reaction rate; n is the order in which the various concentrations of the material react; r is the initial reaction rate of various materials, $moL \cdot L^{-1} \cdot h^{-1}$; and the initial concentration of various materials is C_0, $moL \cdot L^{-1}$.

Table 2. Catalytic activity in the aerobic oxidation of BHMF by different $Au_mPd_n/N\text{-}BN_xC$ nanocatalysts and the Au/Pd content of $Au_mPd_n/N\text{-}BN_xC$.

Sample	BHMF Conversion (%)	HMF Yield (%)	HMFCA Yield (%)	FFCA Yield (%)	FDCA Yield (%)	Pd Content (wt%)	Au Content (wt%)
$Au/N\text{-}BN_2C$	100	0	15.9	3.6	43.9	0	1.58
$Pd/N\text{-}BN_2C$	100	0	40.6	5.8	8.7	1.67	0
$Au_2Pd_1/N\text{-}BN_2C$	100	0	5.5	0	78.9	0.38	1.16
$Au_1Pd_1/N\text{-}BN_2C$	100	0	0	0	95.8	0.63	0.76
$Au_3Pd_1/N\text{-}BN_2C$	100	0	25.7	0	49.6	0.26	1.35
$Au_1Pd_1/N\text{-}BN_1C$	100	0	10.5	3.8	38.9	0.58	0.81
$Au_1Pd_1/N\text{-}BN_3C$	100	0	15.6	4.3	50.6	0.55	0.72

Reaction condition: catalyst = 0.05 g; *n*BHMF: nNa_2CO_3 = 1:4; 100 °C; 24 h; 2.0 MPa O_2.

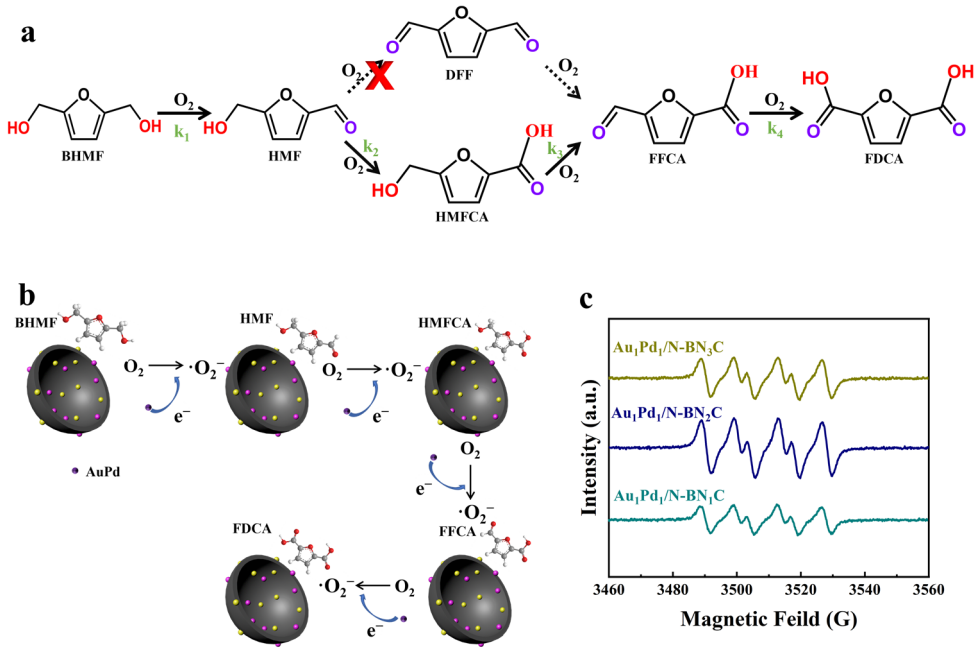

Figure 8. Reaction path of BHMF-catalyzed oxidation to FDCA (**a**), the mechanism of catalytic oxidation of BHMF to FDCA over $Au_mPd_n/N\text{-}BN_xC$ nanocatalysts (**b**), and ESR spectra (superoxide radicals) of $Au_1Pd_1/N\text{-}BN_xC$ (**c**) (x = 1, 2, 3, corresponding to MBA:AM = 1:1, 1:2, 1:3, respectively).

In order to make the calculation more accurate, the determination and calculation were carried out before the rate of substrate conversion was lower than 20% [41]. The results of the experiment showed that the curve of lnC_0-lnr was drawn (Figure S8), and the first-order dynamics constant was obtained (Tables S1–S4). We find that all rate constants

increase with temperature, as we would expect. The Arrhenius equation could be used to determine the activation energy (E_a) and the pre-exponential factor (A):

$$\ln k = \ln A - \frac{E_a}{RT} \quad (2)$$

where k is the rate constant, A is the pre-exponential factor, r is the ideal gas constant, and E_a is the activation energy.

The activation energies of BHMF, HMF, HMFCA, and FFCA were 58.1 kJ·moL^{-1}, 39.1 kJ·moL^{-1}, 129.2 kJ·moL^{-1}, and 56.3 kJ·moL^{-1}, respectively. It was found that the activation energy required for HMFCA conversion to FFCA was the largest, which means that the conversion of HMFCA to FFCA was the rate-determining step of the whole experiment.

ESR spectroscopy with DMPO as the spin-trapping agent was used to further understand the active species involved in the oxidation process of the Au_1Pd_1/N-BN_2C catalyst. As shown in Figure 8c, the characteristic peaks for DMPO-·O_2^- were observed, and the signal intensity of Au_1Pd_1/N-BN_2C was the highest, which had supreme catalytic performance. It is speculated that the formation of reactive oxygen species (·O_2^-) further enhanced catalytic performance [15]. Combined with ESR spectroscopy and catalytic reaction, the selective oxidation mechanism of BHMF was speculated, as shown in Figure 8. The O_2 absorbed at the surface active center of the catalyst was transformed to ·O_2^- by eliminating the electrons deposited on the Au nanoparticles. The interaction of superoxide radicals with water produces OH^-, which promotes the breakage of the C–H bond in the alcohol side chain of the BHMF to yield HMF. In an alkaline environment, OH^- will attack the aldehyde group of HMF, forming an alkoxide ion intermediate (geminal diol). The geminal diol intermediate was subsequently dehydrogenated to generate HMFCA, which was aided by the OH^- absorbed on the surface of Au nanoparticles. Subsequently, HMFCA was converted to FFCA through the same reaction pathway as BHMF, and FFCA was eventually converted to FDCA through the same reaction pathway as HMF.

3. Materials and Methods

3.1. Materials

All of the chemicals were analytical grade and could be utilized right away. Tetraethyl silicate (TEOS), acetonitrile, acrylamide (AM), 3-methacryloxy propyl trimethoxy silane (KH-570), methylene-bis-acrylamide (MBA), 2,2-azobisisobutyronitrile (AIBN), nitric acid (HNO_3), palladium chloride ($PdCl_2$, 99.9%), and gold acid chloride trihydrate ($HAuCl_4·3H_2O$, 99.9%) were acquired from Aladdin Reagent Co., Ltd. (Shanghai, China). Sinopharm Chemical Reagent Co., Ltd. (Shanghai, China) provided the deionized water, ammonium hydroxide (NH_3OH, 25~28%), polyvinyl alcohol (PVA), sodium borohydride ($NaBH_4$, 98%), ethanol, BHMF, HMF, HMFCA, FFCA, FDCA, and sodium carbonate (Na_2CO_3). Acetic acid, methanol, and acetonitrile were high-performance liquid chromatography (HPLC) grade.

3.2. Preparation of the Au_mPd_n/N-BN_xC Nanocatalysts

The specifics involved in preparing the catalysts are described in the Supplementary Materials.

3.3. Catalyst Characterizations

The morphology of samples was distinguished by transmission electron microscopy (TEM), scanning electron microscopy (SEM, Nova TM Nano SEM 230), and high-resolution TEM (HR-TEM). Fourier transform infrared (FT-IR) spectroscopy (Nicolet Nexus 470) was used to observe the changes that occurred in the functional groups of the samples. X-ray diffraction (XRD) was used to examine the samples. The scanning range was 10–80° with a scan speed of 7°·min^{-1}. Raman spectra were evaluated by Renishaw in a Via model Raman microscope with a CCD detector. Nitrogen adsorption–desorption isotherms were utilized in the process of determining Brunauer–Emmett–Teller (BET) surface area. On a Thermo ESCALAB 250 equipped with a monochromatic Al X-ray source, X-ray

photoelectron spectroscopy (XPS) measurements were carried out. Inductively coupled plasma mass spectrometry (ICP-MS, Agilent 7700E) was used to measure the amounts of Au and Pd. Thermogravimetric analysis (TGA) treatment of the catalyst was carried out by heating the catalyst from an ambient temperature to 800 °C (heating rate 5 °C /min) with a Diamond TG/TGA instrument under nitrogen protection. The catalyst was tested via electron paramagnetic resonance (ESR) spectroscopy in deionized water with the same amount of catalyst and DMPO acting as a trapping agent. The resulting solution was sampled at 80 °C for 5 min in an oxygen environment for ESR detection to search the reaction system for reactive oxygen species.

3.4. BHMF Oxidation Reaction

The aerobic transformation of BHMF into FDCA was carried out in a batch-type teflflon-lined stainless-steel autoclave (100 mL). The detailed reaction process was as follows: 50 mg BHMF, 50 mg catalyst, and 16.68 mg Na_2CO_3 were added to a high-pressure reactor containing 40 mL water. The reactor was pressurized to a predetermined pressure and cleaned with oxygen at least three times. After that, the reaction mixture was stirred at 600 rpm and heated to a predetermined temperature. After a fixed reaction time, a certain amount of solution was taken out for centrifugal filtration. On an Agilent 1260 series high-performance liquid chromatograph (HPLC) equipped with a UV detector (280 nm), the liquid product was analyzed with the Agilent TC-C18 column set to 30 °C. The mobile phase had a flow rate of 0.6 $mL \cdot min^{-1}$ and was made up of acetic acid aqueous solution (0.1 wt%) and acetonitrile (*V:V* = 92:8).

The equation that follows was used to calculate the conversion rate of BHMF and the yield of the product.

$$\text{BHMF conversion } (\%) = \frac{\text{moles of reacted BHMF}}{\text{moles of initial BHMF}} \times 100 \quad (3)$$

$$\text{HMF, HMFCA, FFCA, or FDCA yield } (\%) = \frac{\text{moles of HMF, HMFCA, FFCA, or FDCA}}{\text{moles of initial BHMF}} \times 100 \quad (4)$$

In addition, the kinetics of the reaction were studied and calculated through catalytic experiments using BHMF, HMF, HMFCA, and FFCA as substrates.

3.5. Recyclability Test of Catalysts

The optimum reaction conditions were determined by optimizing reaction temperature, pressure, and time. Under ideal conditions, the recyclability of the catalyst for the aerobic oxidation of BHMF to FDCA was investigated. The reaction mixture was used to recover the catalyst through centrifugation and thorough cleaning with an ethanol/deionized water mixture before the catalyst was finally dried completely in a vacuum oven. After that, the recovered catalyst was used in the above method 5 times in a row, and the FDCA yield was recorded each time.

4. Conclusions

In summary, hierarchical porous bowl-like nitrogen-rich carbon-supported bimetallic Au-Pd nanocatalysts (Au_mPd_n/N-BN_xC) with different nitrogen content and bimetal nanoparticle sizes were successfully prepared and employed for the highly efficient aerobic oxidation of BHMF to FDCA. In the catalytic system, BHMF was oxidized to FDCA through three series steps of BHMF→HMF→HMFCA→FFCA→FDCA. Kinetic experiments showed that HMFCA→FFCA was the rate-determining step of this reaction. Oxygen transferred electrons from the nitrogen-doped carbon to the metal surface to form superoxide radicals, which were the active substance of the reaction. The nitrogen-doped carbon support facilitated the dispersity of Au-Pd bimetallic nanoparticles. In particular, the alloying effects in bimetallic Au-Pd nanoparticles favored the catalytic oxidation of the hydroxymethyl and the aldehyde groups, thus improving FDCA yield. Combined

with the synergistic effect of bimetal and metal size, the Au_1Pd_1/N-BN_2C nanocatalyst exhibited the highest catalytic activity, with BHMF conversion of 100% and FDCA yield of 95.8% in sodium carbonate aqueous solution. Moreover, the Au_1Pd_1/N-BN_2C nanocatalyst revealed good stability and could be reused at least five times without a significant loss in catalytic activity. Therefore, this work provides a versatile and promising strategy for the development of heterogeneous catalysts for effective catalytic oxidation of bio-sourced BHMF to FDCA in practical industrial applications.

Supplementary Materials: The following supporting information can be downloaded at: https://www.mdpi.com/article/10.3390/catal13020435/s1.

Author Contributions: Y.L.: methodology, formal analysis, investigation, data curation, writing—original draft preparation, writing—review and editing, and visualization. Y.C. (Yao Chen): conceptualization, investigation, validation, data curation, writing—original draft, writing—review and editing, supervision, and project administration. W.G.: methodology, software, validation, resources, and writing—review and editing. Y.C. (Yu Cao): software and validation. F.W.: validation, resources, and data curation. Y.Z.: conceptualization, methodology, formal analysis, investigation, writing—review and editing, visualization, project administration, and funding acquisition. All authors have read and agreed to the published version of the manuscript.

Funding: This work was financially supported by the Natural Science Foundation of Jiangsu Province (No. BK20180850), the China Postdoctoral Science Foundation (No. 2021M701474), and the Youth Talent Cultivation Plan of Jiangsu University.

Data Availability Statement: The data presented in this study are available upon request from the corresponding author.

Conflicts of Interest: The authors declare no conflict of interest.

Abbreviations

BHMF (2,5-bis(hydroxymethyl)furan); HMF (5-hydroxymethylfurfural); HMFCA (5-hydroxymethyl-2-furancarboxylic acid); FFCA (5-formyl-2-furancarboxylic acid); FDCA (2, 5-furandicarboxylic acid); TPA (terephthalic acid); PET (polyethylene terephthalate); PEF (2,5-furandicarboxylate). Au_mPd_n/N-BN_xC (hierarchical porous bowl-like nitrogen-rich nitrated carbon-supported bimetallic Au-Pd nanocatalysts); AM (acetonitrile, acrylamide); MBA (methylene-bis-acrylamide); TEOS (tetraethyl silicate); KH-570 (3-methacryloxy propyl trimethoxy silane); AIBN (2,2-azobisisobutyronitrile); PVA (polyvinyl alcohol); N-Q (quaternary-N); N-5 (pyrrolic-N); N-6 (pyridinic-N); k (reaction rate constant); n (reaction order); r (initial reaction rate); C_0 (initial concentration); k (rate constant); A (pre-exponential factor); R (ideal gas constant); E_a (activation energy).

References

1. Zhu, B.; Chen, C.L.; Huai, L.Y.; Zhou, Z.Q.; Wang, L.; Zhang, J. 2,5-Bis(hydroxymethyl)furan: A new alternative to HMF for simultaneously electrocatalytic production of FDCA and H_2 over CoOOH/Ni electrodes. *Appl. Catal. B-Environ.* **2021**, *297*, 120396. [CrossRef]
2. Roman-Leshkov, Y.; Chheda, J.N.; Dumesic, J.A. Phase modifiers promote efficient production of hydroxymethylfurfural from fructose. *Science* **2006**, *312*, 1933–1937. [CrossRef] [PubMed]
3. Qureshi, F.; Yusuf, M.; Kamyab, H.; Vo, D.-V.N.; Chelliapan, S.; Joo, S.-W.; Vasseghian, Y. Latest eco-friendly avenues on hydrogen production towards a circular bioeconomy: Current challenges, innovative insights, and future perspectives. *Renew. Sust. Energy Rev.* **2022**, *168*, 112916. [CrossRef]
4. Qureshi, F.; Yusuf, M.; Kamyab, H.; Zaidi, S.; Junaid-Khalil, M.; Arham-Khan, M.; Azad-Alam, M.; Masood, F.; Bazli, L.; Chelliapan, S.; et al. Current trends in hydrogen production, storage and applications in India: A review. *Sustain. Energy Technol.* **2022**, *53*, 102677. [CrossRef]
5. Chen, X.; Yan, N. A brief overview of renewable plastics. *Mater. Today Sustain.* **2020**, *7–8*, 100031. [CrossRef]
6. Mckenna, S.M.; Leimkuehler, S.; Herter, S.; Turner, N.J.; Carnell, A.J. Enzyme cascade reactions: Synthesis of furandicarboxylic acid (FDCA) and carboxylic acids using oxidases in tandem. *Green Chem.* **2015**, *17*, 3271–3275. [CrossRef]
7. Guan, W.; Zhang, Y.L.; Chen, Y.; Wu, J.C.; Cao, Y.; Wei, Y.N.; Huo, P.W. Hierarchical porous bowl-like nitrogen-doped carbon supported bimetallic AuPd nanoparticles as nanoreactors for high efficient catalytic oxidation of HMF to FDCA. *J. Catal.* **2021**, *396*, 40–53. [CrossRef]

8. Siankevich, S.; Savoglidis, G.; Fei, Z.F.; Laurenczy, G.; Alexander, D.T.L.; Yan, N.; Dyson, P.J. A novel platinum nanocatalyst for the oxidation of 5-hydroxymethylfurfural into 2,5-furandicarboxylic acid under mild conditions. *J. Catal.* **2014**, *315*, 67–74. [CrossRef]
9. Zhang, Z.; Deng, K. Recent advances in the catalytic synthesis of 2,5-furandicarboxylic acid and its derivatives. *ACS Catal.* **2015**, *5*, 6529–6544. [CrossRef]
10. Rosenboom, J.-G.; Hohl, D.K.; Fleckenstein, P.; Storti, G.; Morbidelli, M. Bottle-grade polyethylene furanoate from ring-opening polymerisation of cyclic oligomers. *Nat. Commun.* **2018**, *9*, 2701. [CrossRef]
11. Kucherov, F.A.; Gordeev, E.G.; Kashin, A.S.; Ananikov, V.P. Three-dimensional printing with biomass-derived PEF for carbon-neutral manufacturing. *Angew. Chem. Int. Ed.* **2017**, *56*, 15931–15935. [CrossRef]
12. Zhang, Z.; Huber, G.W. Catalytic oxidation of carbohydrates into organic acids and furan chemicals. *Chem. Soc. Rev.* **2018**, *47*, 1351–1390. [CrossRef]
13. Demet, A.E.; Gimello, O.; Arletti, R.; Tanchoux, N.; Sougrati, M.T.; Stievano, L.; Quignard, F.; Centi, G.; Perathoner, S.; Di-Renzo, F. 5-Hydroxymethylfurfural oxidation to 2,5-furandicarboxylic acid on noble metal-free nanocrystalline mixed oxide catalysts. *Catalysts* **2022**, *12*, 814. [CrossRef]
14. German, D.; Pakrieva, E.; Kolobova, E.; Carabineiro, S.A.C.; Stucchi, M.; Villa, A.; Prati, L.; Bogdanchikova, N.; Cortés-Corberán, V.; Pestryakov, A. Oxidation of 5-hydroxymethylfurfural on supported Ag, Au, Pd and bimetallic Pd-Au catalysts: Effect of the support. *Catalysts* **2021**, *11*, 115. [CrossRef]
15. Zhang, Y.L.; Cao, Y.; Yan, C.H.; Liu, W.Y.; Chen, Y.; Guan, W.; Wang, F.; Liu, Y.R.; Huo, P.W. Rationally designed Au-ZrO_x interaction for boosting 5-hydroxymethylfurfural oxidation. *Chem. Eng. J.* **2023**, *459*, 141644. [CrossRef]
16. Pichler, C.M.; Al-Shaal, M.G.; Gu, D.; Joshi, H.; Ciptonugroho, W.; Schueth, F. Ruthenium supported on high-surface-area zirconia as an efficient catalyst for the base-free oxidation of 5-hydroxymethylfurfural to 2,5-furandicarboxylic acid. *ChemSusChem* **2018**, *11*, 2083–2090. [CrossRef]
17. Rass, H.A.; Essayem, N.; Besson, M. Selective aqueous phase oxidation of 5-hydroxymethylfurfural to 2,5-furandicarboxylic acid over Pt/C catalysts: Influence of the base and effect of bismuth promotion. *Green Chem.* **2013**, *15*, 2240–2251. [CrossRef]
18. Naim, W.; Schade, O.R.; Saraci, E.; Wuest, D.; Kruse, A.; Grunwaldt, J.D. Toward an intensified process of biomass-derived monomers: The influence of 5-(hydroxymethyl)furfural byproducts on the gold-catalyzed synthesis of 2,5-furandicarboxylic acid. *ACS Sustain. Chem. Eng.* **2020**, *8*, 11512–11521. [CrossRef]
19. Megias-Sayago, C.; Chakarova, K.; Penkova, A.; Lolli, A.; Ivanova, S.; Albonetti, S.; Cavani, F.; Antonio-Odriozola, J. Understanding the role of the acid sites in 5-hydroxymethylfurfural oxidation to 2,5-furandicarboxylic acid reaction over gold catalysts: Surface investigation on $Ce_xZr_{1-x}O_2$ compounds. *ACS Catal.* **2018**, *8*, 11154–11164. [CrossRef]
20. Zhang, Z.; Zhen, J.; Liu, B.; Lv, K.; Deng, K.J. Selective aerobic oxidation of the biomass-derived precursor 5-hydroxymethylfurfural to 2,5-furandicarboxylic acid under mild conditions over a magnetic palladium nanocatalyst. *Green Chem.* **2015**, *17*, 1308–1317. [CrossRef]
21. Wang, Y.; Yu, K.; Lei, D.; Si, W.; Feng, Y.J.; Lou, L.L.; Liu, S.X. Basicity-tuned hydrotalcite-supported Pd catalysts for aerobic oxidation of 5-hydroxymethyl-2-furfural under mild conditions. *ACS Sustain. Chem. Eng.* **2016**, *4*, 4752–4761. [CrossRef]
22. Jin, M.; Yu, L.; Chen, H.; Ma, X.L.; Cui, K.; Wen, Z.; Ma, Z.W.; Sang, Y.S.; Chen, M.M.; Li, Y.D. Base-free selective conversion of 5-hydroxymethylfurfural to 2,5-furandi-carboxylic acid over a CoO_x-CeO_2 catalyst. *Catal. Today* **2021**, *367*, 2–8. [CrossRef]
23. Davis, S.E.; Houk, L.R.; Tamargo, E.C.; Datye, A.K.; Davis, R.J. Oxidation of 5-hydroxymethylfurfural over supported Pt, Pd and Au catalysts. *Catal. Today* **2011**, *160*, 55–60. [CrossRef]
24. Lei, D.; Yu, K.; Li, M.-R.; Wang, Y.L.; Liu, T.; Liu, P.K.; Lou, L.L.; Wang, G.C.; Liu, S.X. Facet effect of single-crystalline Pd nanocrystals for aerobic oxidation of 5-hydroxymethyl-2-furfural. *ACS Catal.* **2017**, *7*, 421–432. [CrossRef]
25. Wan, X.; Zhou, C.; Chen, J.S.; Deng, W.P.; Zhang, Q.H.; Yang, Y.H.; Wang, Y. Base-free aerobic oxidation of 5-hydroxymethyl-furfural to 2,5-furandicarboxylic acid in water catalyzed by functionalized carbon nanotube-supported Au-Pd alloy nanoparticles. *ACS Catal.* **2014**, *4*, 2175–2185. [CrossRef]
26. Wei, Y.N.; Zhang, Y.L.; Chen, Y.; Wang, F.; Cao, Y.; Guan, W.; Li, X. Crystal faces-tailored oxygen vacancy in Au/CeO_2 catalysts for efficient oxidation of HMF to FDCA. *ChemSusChem* **2022**, *15*, e202101983. [CrossRef]
27. Lin, G.B.; Lin, W.W.; Wu, J.H.; Zhan, Y.; Okejiri, F.; Weng, M.G.; Fu, J. Oxidation of 5–methoxymethylfurfural to 2, 5-furandicarboxylic acid over Ru/hydroxyapatite catalyst in water. *Chem. Eng. Sci.* **2022**, *249*, 117343. [CrossRef]
28. Guan, W.; Chen, C.; Li, B.; Chen, Y.; Wei, Y.N.; Cao, Y.; Wang, F.; Yan, Y.S.; Liu, B.; Zhang, Y.L. Pickering high internal phase emulsions templated CoO_x-HPC loading bimetallic AuPd nanoparticles for catalytic oxidation of 5-hydroxymethylfurfural to 2, 5-furan dicarboxylic. *ChemistrySelect* **2022**, *7*, e202104058. [CrossRef]
29. Antonietti, M.; Lopez-Salas, N.; Primo, A. Adjusting the structure and electronic properties of carbons for metal-free carbocatalysis of organic transformations. *Adv. Mat.* **2019**, *31*, 1805719. [CrossRef]
30. Hu, X.W.; Fan, M.Y.; Zhu, Y.Y.; Zhu, Q.; Song, Q.; Dong, Z.P. Biomass-derived phosphorus-doped carbon materials as efficient metal-free catalysts for selective aerobic oxidation of alcohols. *Green Chem.* **2019**, *21*, 5274–5283. [CrossRef]
31. Guo, Z.W.; Zheng, J.; Li, B.R.; Da, Z.L.; Meng, M.J. Fabrication of mixed matrix membranes blending with the TiO_2/Bi_3O_4Cl 2D/2D heterojunction for photocatalytic degradation of tetracycline. *Appl. Surf. Sci.* **2022**, *574*, 151549. [CrossRef]
32. Ferraz, C.P.; Zielinski, M.; Pietrowski, M.; Heyte, S.; Dumeignil, F.; Rossi, L.M.; Wojcieszak, R. Influence of support basic sites in green oxidation of biobased substrates using Au-promoted catalysts. *ACS Sustain. Chem. Eng.* **2018**, *6*, 16332–16340. [CrossRef]

33. Guan, W.; Zhang, Y.L.; Yan, C.H.; Chen, Y.; Wei, Y.N.; Cao, Y.; Wang, F.; Huo, P.W. Base-free aerobic oxidation of furfuralcohols and furfurals to furancarboxylic acids over nitrogen-doped carbon-supported AuPd bowl-like catalyst. *ChemSusChem* **2022**, *15*, e202201041. [CrossRef]
34. Xiang, Z.H.; Cao, D.P.; Huang, L.; Shui, J.L.; Wang, M.; Dai, L.M. Nitrogen-doped holey graphitic carbon from 2D covalent organic polymers for oxygen reduction. *Adv. Mater.* **2014**, *26*, 3315. [CrossRef]
35. Wang, H.B.; Maiyalagan, T.; Wang, X. Review on recent progress in nitrogen-doped graphene: Synthesis, characterization, and its potential applications. *ACS Catal.* **2012**, *2*, 781–794. [CrossRef]
36. Liu, X.Y.; Zhang, M.; Li, Z.H. CoO_x-MC (MC = Mesoporous Carbon) for highly efficient oxidation of 5-hydroxymethylfurfural (5-HMF) to 2,5-furandicarboxylic acid (FDCA). *ACS Sustain. Chem. Eng.* **2020**, *8*, 4801–4808. [CrossRef]
37. Villa, A.; Schiavoni, M.; Campisi, S.; Veith, G.M.; Prati, L. Pd-modified Au on carbon as an effective and durable catalyst for the direct oxidation of HMF to 2,5-furandicarboxylic acid. *ChemSusChem* **2013**, *6*, 609–612. [CrossRef]
38. Lee, K.-U.; Byun, J.Y.; Shin, H.-J.; Kim, S.H. Nanoporous gold-palladium: A binary alloy with high catalytic activity for the electro-oxidation of ethanol. *J. Alloys Compd.* **2020**, *842*, 155847. [CrossRef]
39. Yan, W.; Tang, Z.H.; Wang, L.K.; Wang, Q.N.; Yang, H.Y.; Chen, S.W. PdAu alloyed clusters supported by carbon nanosheets as efficient electrocatalysts for oxygen reduction. *Int. J. Hydrogen Energy* **2017**, *42*, 218–227. [CrossRef]
40. Li, X.; Tong, Z.K.; Zhu, S.; Deng, Q.; Chen, S.X.; Wang, J.; Zeng, Z.L.; Zhang, Y.L.; Zou, J.J.; Deng, S.J. Water-mediated hydrogen spillover accelerates hydrogenative ring-rearrangement of furfurals to cyclic compounds. *J. Catal.* **2022**, *405*, 363–372. [CrossRef]
41. Yusuf, M.; Beg, M.; Ubaidullah, M.; Shaikh, S.F.; Keong, L.K.; Hellgardt, K.; Abdullah, B. Kinetic studies for DRM over high-performance Ni–W/Al_2O_3–MgO catalyst. *Int. J. Hydrogen Energy* **2022**, *47*, 42150–42159. [CrossRef]